First-principles study on the effects of twin boundaries on anodic dissolution of Mg

Hui Ma,[1] Min Liu,[1] Weiliang Chen,[1,2] Changgang Wang,[1] Xing-Qiu Chen,[1,*] Junhua Dong,[1,†] and Wei Ke[1]
[1]*Environmental Corrosion Center and Shenyang National Laboratory for Materials Science (SYNL), Institute of Metal Research, Chinese Academy of Sciences, Shenyang 110016, China*
[2]*School of Metallurgy, Northeastern University, Shenyang, Liaoning 110819, China*

(Received 11 December 2018; revised manuscript received 19 March 2019; published 17 May 2019)

Known experiments revealed that various deformation-induced defects in wrought Mg-based alloys indeed accelerate the corrosion rate. In particular, for Mg-based alloys the twinning mode under plastic deformation is the usually and more easily occurring one than other defects. However, to date it has been very difficult to study the specific effect of twin boundaries (TBs) on the corrosion behavior of Mg-based alloys due to the coexistence of other defects in wrought alloy. Here, through first-principles calculations we have theoretically investigated the effects of TBs on the anodic dissolutions of Mg metal. It has been found that the presence of various TBs (TB1$\{10\bar{1}1\}[1\bar{2}10]$, TB2 $\{10\bar{1}2\}[1\bar{2}10]$, or TB3 $\{10\bar{1}3\}[1\bar{2}10]$) accelerates the corrosion rate and the TB-induced accelerations of the corrosion current density are indeed correlated with the TB interfacial length per area. Physically, the existence of the TBs on the specified surfaces increases the surface energy density, which implies that atoms at various TB-containing surfaces become less stable in energy as compared with the TB-free surface. In addition, we have analyzed that some alloying elements (As, Cd, Hg, Zn, and Sn) in combination with TBs can reduce the anodic dissolution rate, potentially enhancing the corrosion resistance of Mg-based alloys.

DOI: 10.1103/PhysRevMaterials.3.053806

Magnesium alloys are being widely applied in industries mainly because of their light weight and high strength [1–8]. In combination with the alloying control and the heat treatment process, the wrought magnesium alloys exhibit higher strength, better ductility, and even more diversified mechanical properties to satisfy the requirements of various engineering applications. However, the poor corrosion resistance heavily hinders their wide applications in many industrial fields. Mg can be easily oxidized into MgO in the air and heavily corroded even in the neutral solution due to its extremely low standard electrode potential (about $-2.37\,V_{SHE}$) [9,10]. Within this context, in order to improve their corrosion resistances, a large number of investigations [1–8,11–17] had been performed to study the corrosion behaviors of magnesium alloys. Concerning wrought magnesium alloys, there exist a lot of deformation-induced defects, such as dislocations and deformation twins [18–23]. These defects had been revealed to directly influence the corrosion behaviors of magnesium alloys. For instance, the deformation-induced defects were found to accelerate the corrosion rates of Mg-Zn [18], AZ31D [20], AZ31B [24], ZE41 [25], AM50, and AZ91D [19] alloys, as well as pure Mg [26]. Even the galvanic corrosion between some twinned and untwinned areas in AZ31 alloys was evidenced as well [22].

From the experimental point of view, those studies [18–20,22,24–26] revealed the general observation that various deformation-induced defects in wrought magnesium alloys indeed accelerate the occurrence of corrosion. However, it would be extremely difficult to elucidate the effect of any individual deformation-induced defect on the corrosion behaviors because (i) those wrought magnesium alloys contain different alloying elements and (ii) various deformation-induced defects can possibly, simultaneously, coexist. In general, during the plastic deformation process of magnesium alloys the twinning mode is usually the one that occurs more easily than the other types of defects because Mg is a typical hcp metal with fewer slip systems [27]. Although the common knowledge is that in a corrosive environment all types of grain boundaries in Mg are more active than the grain bulk [28], the influence of the deformation-induced twins, one of the most important defects in wrought magnesium alloys, on corrosion has been remained unknown. Hence, it is highly desirable to study the relationship between the deformation-induced twins and the corrosion of magnesium alloys, further elucidating their intrinsic mechanisms and guiding the design of high-performance corrosion-resistant magnesium alloys.

It is well known that the electrochemical corrosion behavior of Mg is highly complicated. The anodic reaction of Mg usually exhibits the anodic dissolution and the generation of hydrogen, which is the so-called negative difference effect (NDE) [29]. The corrosion of Mg was hence supposed to proceed notionally under "cathodic control" [30,31]. A number of theoretical works were focused on the adsorption of water molecules [32,33], of hydrogen atoms [34,35], and of other particles [36,37] on the Mg surfaces to elucidate the electrochemical corrosion of Mg. In fact, it is worth noting that the electrochemical corrosion is the coupling effect between the anodic and cathodic reactions, and both of them play important roles in the behaviors of the electrochemical corrosion. The corrosion first occurs on the surfaces of materials and hence the surface states (including the crystal orientations, the crystal defects, and the segregation of

*Corresponding author: xingqiu.chen@imr.ac.cn
†Corresponding author: jhdong@imr.ac.cn

alloying elements) directly influence the corrosion rate. In addition, the recent studies revealed that the anodic reaction governs the orientation-dependent corrosion behavior of Mg [38]. The anisotropic corrosion behavior of Mg was theoretically estimated by using the surface energy [39]. However, the estimated differences of the corrosion rates upon different orientated surfaces were much higher than the experimentally observed ones [39]. Mechanically, it was not enough to alone estimate the activation energy in the dissolution kinetics of Mg with the energy of the topmost surface layer.

Most recently, in order to simulate the corrosion-resistant behavior of materials in a corrosive environment, we have developed first-principles modeling of anodic dissolution of metals and alloys [40]. This modeling method is used to estimate the electrode potential (U) of materials and the current density (I) by combining some necessary parameters mainly derived from first-principles calculations. This method provides an accessible tool to investigate the influences of various defects on anodic dissolution behaviors, only with necessary first-principles inputs including defects considered in the structural modeling. In combination with our modeling methods, here we intend to investigate the effects of the deformation-induced twins on the anodic dissolution of magnesium alloys. In order to construct the corresponding structural models for first-principles calculations by including twin boundaries (TBs), we first need to clarify the TB structures in hcp Mg alloys.

To date, there has been a large number of theoretical studies of (i) TBs in hcp metals (i.e., Ti [41], Be [42], Mg [43], etc.) and (ii) the behaviors of various solute alloying atoms at TBs and their related segregation energies [27,44,45]. Taking an example, the experiment of the high-angle annular dark-field scanning transmission electron microscopy (HAADF-STEM) indicated the existence of some TBs of Mg-Gd-Zn alloys. Most of the TBs were evidenced to be $\{10\bar{1}1\}$, but both $\{10\bar{1}2\}$ and $\{10\bar{1}3\}$ twins were also observed under the larger compression strains [27]. Furthermore, the segregation of solutes, Gd and Zn, at these three TBs was computationally analyzed using first-principles calculations in combination with experimental observations [27], evidencing their periodic segregation in the fully coherent TBs in Mg-Gd-Zn alloys.

In this work, through first-principles calculations [46,47] we have mainly investigated the effects of three TBs, TB1 $\{10\bar{1}1\}[1\bar{2}10]$, TB2 $\{10\bar{1}2\}[1\bar{2}10]$, and TB3 $\{10\bar{1}3\}[1\bar{2}10]$ (where the $\{10\bar{1}x\}(x = 1\text{–}3)$ is the twinning plane, and the $[1\bar{2}10]$ is the rotation axis), on the anodic dissolution of Mg in a pH = 9.7 corrosive environment. In order to correctly derive both the current density and the electrode potential for anodic dissolutions within the framework of our modeling method [40], we need to derive some necessary parameters of the surface energy density (E_{surf}/ρ), the surface energy (E_{surf}), and the work function (Φ) of the TB-containing surfaces with the consideration of the effects of three TBs on the rate of anodic dissolution of pure Mg. Furthermore, the effects of some alloying elements (Al, As, Cd, Cr, Ga, Hg, Mn, Zn, Zr, and Sn) on the anodic dissolution rates have been also analyzed upon TBs or grain bulk.

I. COMPUTATIONAL DETAILS AND MODELING

The computational details of density functional theory (DFT) by employing the Vienna Ab initio Simulation Package (VASP) [48,49] have been already given in Ref. [40]. Here, we still emphasize three important details for our current calculations. In the first, the exchange-correlation function was dealt with via the projector augmented wave (PAW) [50] method and generalized gradient approximation (GGA) within the Perdew-Burke-Ernzerhof (PBE) approach [51]. In the second, the plane-wave cutoff energy was set to 300 eV, which was tested to be high enough for Mg for accurate electronic optimization. In the third, the criterion of the force convergence was below 0.0001 eV/Å and 0.01 eV/Å for the structural and ionic relaxations of bulk and the surfaces, respectively.

On the base of fully relaxed unit cells, we built three TBs (TB1 $\{10\bar{1}1\}$, TB2 $\{10\bar{1}2\}$, and TB3 $\{10\bar{1}3\}$) using the appropriate symmetry operation following previous works [27,43,52], as shown in Fig. 1. The supercells contain 40, 40, and 48 atoms, for TBs $\{10\bar{1}1\}$, $\{10\bar{1}2\}$, and $\{10\bar{1}3\}$, respectively. For the three TB structures, all atomic positions and the lattice parameters are fully relaxed to a convergent configuration by minimizing the forces (below 0.01 eV/Å). The Brillouin zones of the three TBs are sampled by the $17 \times 5 \times 2$, $17 \times 7 \times 2$, and $17 \times 3 \times 3$ $\vec{k}$-point meshes generated using the Monkhorst-Pack scheme [53], respectively. The energy of the TB (E_{TBs}) is usually used to evaluate the stability of a twin boundary, which can be computed by

$$E_{\text{TBs}} = \frac{E_{\text{supercell}}(n) - nE_{\text{bulk}}}{2S}, \tag{1}$$

where $E_{\text{supercell}}(n)$ is the total energy of a supercell containing a specified twin boundary with n atoms, E_{bulk} is a reference

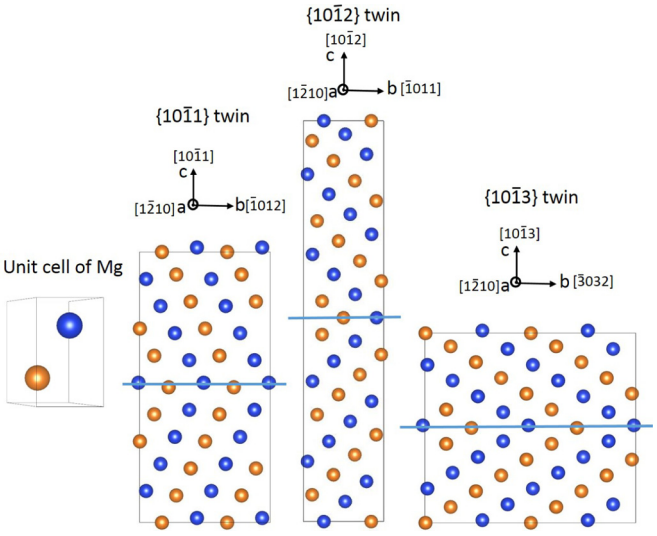

FIG. 1. The unit cell lattice structure of Mg and its supercells containing three different TBs. The supercells contain 40, 40, and 48 atoms for $\{10\bar{1}1\}$, $\{10\bar{1}2\}$, and $\{10\bar{1}3\}$ twin boundaries, respectively. The thick blue lines in the middle of supercells represent traces of TBs. To visualize the twin boundaries more clearly, we distinguish the different atoms in color on different basal planes.

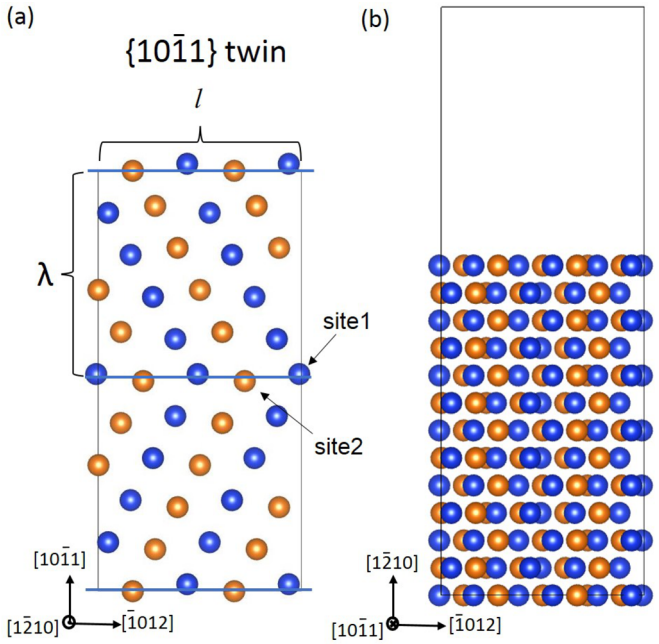

FIG. 2. Surface slab structural modeling with TB {10$\bar{1}$1} on the (1$\bar{2}$10) surface: (a) top and (b) front view of the modeling. The thick blue line in the middle of the supercell represents the trace of TB {10$\bar{1}$1}. Sites 1 and 2 denote the compressed site and the extended site on the grain boundary plane, respectively.

energy of the bulk system (given per atom), and S is a TB's interface area for the TB-containing structural model. Note that for TBs in our structural models we have considered two of the same interfaces due to the lattice periodicity.

Generally, the surface states of the experimental samples are very complex, including various crystalline-orientation surfaces and defects. However, due to the huge time-consuming computations it is very difficult to simulate the real surface considering all these possible situations mentioned above in a material, simultaneously. In our current modeling, we have only focused on the effect of the deformation twins on the corrosion of Mg. For the sake of this purpose, we have built surface structural models containing only one TB. Specifically, after full relaxations and structural optimizations of three TBs, we have built surface slab models along the a axis of the TB supercells (namely, along the [1$\bar{2}$10] direction of the hcp Mg structure) to simulate the surface (1$\bar{2}$10) containing the three different TBs {10$\bar{1}$1}, {10$\bar{1}$2}, and {10$\bar{1}$3}, respectively. In these models, the vacuum lengths are set to 15 Å and all the twin boundary planes are perpendicular to the given surface. Figure 2 shows the surface slab model with a TB1 {10$\bar{1}$1} on surface (1$\bar{2}$10). All three TB-containing surface slab models contain 13 atomic layers, which is enough to simulate the surface and to calculate surface energy [54,55]. When relaxing the surface slab structures, the five atomic layers in the middle of the slab models are kept fixed to their bulk positions during the calculations, and other layers on both sides are allowed to fully relax to optimize the lowest-energy configurations. The $5 \times 2 \times 1$, $7 \times 2 \times 1$, and $3 \times 3 \times 1$ $\vec{k}$-point meshes generated using the Monkhorst-Pack scheme [53] are used to sample the Brillouin zones for the slab models containing TB1, TB2, and TB3, respectively. In addition, the (1$\bar{2}$10) surface without any TB is also included as a reference to elucidate the effect of TBs on the anodic dissolution behavior.

Because the density of TBs on the surface directly influences the effect of the TB on the corrosion rate, we need to introduce a reasonable parameter to define the density of TBs on the given surface. In experiment, some works [56,57] have defined the volume fraction (f) of a twin boundary by considering the width (t) of twins, and the average distance (λ) between twins through the equation $f = \frac{t}{t+\lambda}$. However, in our calculation, it is difficult to define the width (t) of twins in the structure model of a TB-containing supercell. Therefore, following the previous work [58] we introduce a quantity L_s, the interface length per unit area, to express the density of the TB on the (1$\bar{2}$10) surface:

$$L_s = \frac{2l}{2l\lambda} = \frac{1}{\lambda}, \tag{2}$$

where l is the length of the interface on the surface (1$\bar{2}$10), and two interfaces are considered due to the lattice periodicity. λ is the distance between the two twins, as marked in Fig. 2(a). For these three TB-containing surface structures used here, the interface lengths per unit area (marked as L_s^0) are shown in Table III.

According to our anodic dissolution modeling in a corrosive environment [40], the relationship between the current density (I) of the anodic dissolution and the electrode potential (U) in a corrosive environment can be written as

$$I = I_0 \left\{ \exp\left[\frac{\alpha n F (U - U_e)}{RT}\right] - \exp\left[-\frac{(1-\alpha) n F (U - U_e)}{RT}\right] \right\}, \tag{3}$$

where n is the number of electrons involved in the electrochemical reaction and K, h, F, R, and T are the Boltzmann constant, Planck constant, Faraday constant, gas constant, and absolute temperature, respectively. The parameter α is a transfer coefficient, which is 0.36 for anodic dissolution of Mg alloy by fitting the Tafel line according to the experimental measurement [40,59], and we suppose that it is the same for TB-containing and TB-free surfaces. The equilibrium potential of the anodic dissolution reaction, $U_e = \frac{\Phi + \Delta\Phi}{e}$ [60], is determined by the work function (Φ) of a given material surface and its invariant $\Delta\Phi$ imposed by (i) the interactions between the solution and the metal surface and (ii) various crystal surface defects (i.e., vacancy and grain boundary, etc.), surface alloying, reconstructions, and external adsorption. In our current work, we have mainly focused on the effect of the deformed twin boundary on the electrochemical dissolution rate and ignored the interactions between the aqueous environment and the metallic surface.

The equilibrium exchange current density I_0 in Eq. (3) reads

$$I_0 = nF \frac{KT}{h} \exp\left(-\frac{\Delta G^0}{RT}\right) \exp\left[\frac{\alpha n(\Phi + \Delta\Phi)}{KT}\right] \times \exp\left(\frac{E_{\text{surf}}}{\rho KT}\right), \tag{4}$$

where E_{surf} is the surface energy, E_{surf}/ρ is the surface energy density, and $\Phi + \Delta\Phi$ is the work function and its invariant for the TB-containing surface slab models. n is the number of electrons involved in the process from a Mg atom to a Mg ion. In the literature, during the anodic dissolution process of Mg, there have been two main suggested mechanisms. The first one is that the monovalent Mg^+ is commonly considered an intermediate state [9,61–66], and the second one is that Mg prefers to dissolve into Mg^{2+} directly [67,68]. In fact, according to our DFT calculations, it is very difficult for a Mg atom to, simultaneously and directly, lose its two valence electrons, because we have derived the energy required for the formation Mg^{2+} and Mg^+ ions through the expressions as follows:

$$\text{Mg} \rightarrow \text{Mg}^{2+} + 2e, \quad \text{Mg} \rightarrow \text{Mg}^{+} + e.$$

Our calculations have demonstrated that the required energy for the direct formation of Mg^{2+} is higher than that for the formation of the intermediate monovalent Mg^+ ion. Hence, it is more difficult for a free Mg atom to lose its two electrons, simultaneously. Following these calculations, here we have supposed $n = 1$ for Mg in the intermediate transition state of the anodic dissolution. Once this intermediate state of monovalent magnesium is formed, it will quickly continue to lose another electron to form the stable Mg^{2+} ion in the solution. The parameter of ΔG^0, part of the activation energy, which is only related to the material itself, is about 3.03 eV for Mg-based alloys [40].

To establish the correlation between the current density and the electrode potential, we need to clarify the two important parameters of the work function Φ and surface energy density E_{surf}/ρ. The work function is a reflection of the Fermi level for a surface structure in the slab model, which can be computed by the difference between the energy of the vacuum region far from the surface (V_e) and the Fermi energy (E_f) of a slab model as $\Phi = V_e - E_f$. For the surface energy density E_{surf}/ρ of a given surface, E_{surf} is the surface energy and $\rho = \frac{N}{A}$ is the surface atom density, where N is the total atom number within the surface area A. In particular, this number N is not the atomic number on the topmost single layer of a slab model. Because a few layers of atoms in the vicinity of the surface contribute to the surface energy, it is highly necessary to define a reasonable number of surface atoms, N, by including a few layers.

It is noteworthy that, when the difference between U and U_e is large enough (namely, $U \gg U_e$), the current density, I, in Eq. (2) can be simplified as

$$I = I_0 \exp\left[\frac{\alpha n F(U - U_e)}{RT}\right]. \tag{5}$$

By combining Eq. (4) into Eq. (5), the Tafel straight line can be expressed in the logarithmic form as

$$\ln I = \ln\left(nF\frac{KT}{h}\right) + \frac{\alpha n F U - \Delta G^0}{RT} + \frac{E_{\text{surf}}}{\rho KT}. \tag{6}$$

In Eq. (6), within the region of the Tafel line the surface energy density E_{surf}/ρ becomes a key factor in determining the rate of the anodic dissolution. This equation implies that, with the situation of $U \gg U_e$ in the region of the Tafel line, the rate of the anodic dissolution has nothing to do with the equilibrium potential of U_e and, thereby, also with the work function of Φ.

Furthermore, we have investigated the influence of alloying solutes (X) at the TBs on the anodic dissolution behaviors of magnesium alloys. In the first, we have calculated the segregation energy of each considered solute, X, on site 1 or site 2 of the surface slab model with a selected TB1 $\{10\bar{1}1\}$ (Fig. 2) to find their energetically favorable site. Note that the segregation energy at the TBs in the previous publication [27] was defined to be a required energy without any consideration of specified surfaces in structural modeling, with an aim of clarifying the tendency of the solutes to move from the bulk to the grain boundary region. However, because we have treated the problem of corrosion in our current modeling, we have to consider the situation of the specified surface in which the TBs exist and the solute X locates at the TBs. Therefore, it is necessary to identify whether the solute X prefers to locate at the TBs on the specified surface. In order to discuss this possibility, we have defined the segregation energy of the solute X at the TBs on the given surface with respect to its bulk phase as follows:

$$E_{\text{seg}}^{\text{TB}}(X) = \frac{1}{m}\Big\{\Big[E_{\text{slab}}^{\text{TB}}\big(\text{Mg}_{\langle N-m\rangle}X_m^{\text{TB}}\big) - E_{\text{slab}}^{\text{TB}}(\text{Mg}_N)\Big] - m[E_{\text{bulk}}(\text{Mg}_{\langle Z-1\rangle}X) - ZE_{\text{bulk}}(\text{Mg})]\Big\}, \tag{7}$$

where $E_{\text{slab}}^{\text{TB}}(\text{Mg}_{\langle N-m\rangle}X_m^{\text{TB}})$ is the calculated total energy of the TB-containing slab model with m alloying X atoms at site 1 or 2 of the TB and $N - m$ Mg atoms. The $E_{\text{slab}}^{\text{TB}}(\text{Mg}_N)$ is the calculated total energy of the TB-containing slab model without the X alloying addition. The term $E_{\text{bulk}}(\text{Mg}_{\langle Z-1\rangle}X)$ is the calculated total energy of the alloyed supercell in its bulk phase including $Z - 1$ Mg atoms and one solute X atom, and the $E_{\text{bulk}}(\text{Mg})$ is the energy of the hcp Mg metal per atom. Similarly, we have defined the segregation energy of the solute X on the ideal surface without any TBs with respect to its bulk phase as follows:

$$E_{\text{seg}}^{\text{surf}}(X) = \frac{1}{m}\Big\{\Big[E_{\text{slab}}^{\text{ideal}}(\text{Mg}_{\langle N-m\rangle}X_m) - E_{\text{slab}}^{\text{ideal}}(\text{Mg}_N)\Big] - m[E_{\text{bulk}}(\text{Mg}_{\langle Z-1\rangle}X) - ZE_{\text{bulk}}(\text{Mg})]\Big\}, \tag{8}$$

where $E_{\text{slab}}^{\text{ideal}}(\text{Mg}_{\langle N-m\rangle}X_m)$ is the total energy of the alloyed TB-free surface slab, which has $N - m$ Mg atoms and m solute X atoms, and $E_{\text{slab}}^{\text{ideal}}(\text{Mg}_N)$ is the total energy of the TB-free surface slab including N Mg atoms. By comparing $E_{\text{seg}}^{\text{TB}}(X)$ with $E_{\text{seg}}^{\text{surf}}(X)$, we can know whether or not the alloying X atom prefers to locate at the TBs on the given surface. In the slab model, both N and Z are equal to 260, and the number of alloyed X atoms, m, is 2 due to the symmetric geometry in the slab model.

Using these constructed slab models with the large enough vacuum, we have derived the surface energies (E_{surf}), the surface energy densities (E_{surf}/ρ), and the work functions (Φ) with m X-alloyed modeling to elucidate the effect of segregation solutes on anodic dissolution behaviors according to our previous modeling [40]. In the treatment with the effect of environment, we have supposed a relatively ideal solution as compared with reality. Specifically, we have assumed the hydrogen evolution reaction as the cathodic reaction, which depends on the pH value of the solution. We have not

considered the effect of other ions and the existence of the oxidation film.

II. RESULTS AND DISCUSSIONS

Through first-principles calculations, we have derived the energies of three TBs considered here. As illustrated in Table I, the calculated energies of TB1 $\{10\bar{1}1\}$, TB2 $\{10\bar{1}2\}$, and TB3 $\{10\bar{1}3\}$ are 85.56, 111.94, and 209.92 mJ/m^2, respectively. Note that for both TB1 and TB2 our current calculated values are in a nice agreement with previously calculated data [27,43,52]. However, for TB3 there were no available reported data in the literature. It has been noted that the energy of the TB1 is the lowest among them, followed by the TB2 and the highest being the TB3. Their stabilities can be interpreted well by the degree of the disordered arrangement of atoms at their TBs. In terms of the coincidence site lattice (CSL) theory [69,70], the more coincidence sites at the grain boundary (namely, the two grains at the grain boundary share the more common atoms), the smaller the distortion degree of the atomic arrangement. It thereby lowers the energy of the grain boundary. The atomic density in the TB plane decreases as the TB plane goes from TB1 to TB3. This fact implies that the two grains at the TB1 $\{10\bar{1}1\}$ share more atoms, thereby making its energy become relatively lower.

Furthermore, we have derived three main parameters of the surface energies (E_{surf}), the surface energy densities (E_{surf}/ρ), and the work functions (Φ) of these TB-containing $(1\bar{2}10)$ surfaces according to our anodic dissolution modeling in a corrosive environment. In order to compare the TB-containing effects, we have also derived the corresponding parameters for the TB-free surface $(1\bar{2}10)$ as a reference. As illustrated in Table II, the existence of TBs makes the surface energies for all three TB-containing surfaces higher than that of the TB-free $(1\bar{2}10)$ surface. It is mainly because the atoms at TBs are rearranged to form the twin defects under necessary distortions. In addition, the twin formation indeed changes the local coordinators of atoms at the TBs. The calculated work functions of the TB1- and TB2-containing surfaces are even a bit larger than that of the perfect one, whereas the TB3-containing surface is slightly smaller (Table II).

By combining Eq. (3) and Eq. (4) and using the specified parameters in Table II according to our modeling [40], we have derived the polarization curves of the anodic dissolutions of the specified TB-containing $(1\bar{2}10)$ surfaces (TB1 $\{10\bar{1}1\}$, TB2 $\{10\bar{1}2\}$, and TB3 $\{10\bar{1}3\}$) in comparison with its TB-free surface $(1\bar{2}10)$ of pure Mg in Fig. 3. The anodic dissolution polarization curves for the TB-containing surfaces certainly are clearly shifted to the right with respect to the TB-free $(1\bar{2}10)$ surface. Under the same potential the current densities of the TB-containing surfaces indeed become larger than that of the TB-free surface. This fact means that the existence of TBs on the surface speeds up the anodic dissolution behavior. In other words, Mg atoms in three TB-containing surfaces would unavoidably dissolute more easily within a corrosive environment in comparison with the TB-free surface. This kind of behavior is certainly reflected well by the elevated surface energy densities of the TB-containing surfaces (Table II) because the atoms on them become less stable, thermodynamically.

In order to obtain the corrosion potential and corrosion current density, it is certainly necessary to include a hydrogen evolution reaction as the depolarization reaction according to our modeling [40]. It is clear that the experimental observations were performed for the AM50 alloy in a sodium tetraborate solution (pH = 9.7) and the polarization curves

TABLE I. DFT-derived energies (E_{TBs}) of the three twin boundaries (TB1 $\{10\bar{1}1\}$, TB2 $\{10\bar{1}2\}$, and TB3 $\{10\bar{1}3\}$) compared with previous calculated data.

	E_{TBs} (mJ/m^2)	
TBs	This work	Others
TB1: $\{10\bar{1}1\}$	85.6	84.2 [43]
TB2: $\{10\bar{1}2\}$	111.9	118.8 [43], 114 [52], 129.1 [27]
TB3: $\{10\bar{1}3\}$	209.9	

TABLE II. DFT-derived surface energies (E_{surf}), surface energy densities (E_{surf}/ρ), and work functions (Φ) for TB-free surface $(1\bar{2}10)$, and the specified TB-containing $(1\bar{2}10)$ surfaces (TB1 $\{10\bar{1}1\}$, TB2 $\{10\bar{1}2\}$, and TB3 $\{10\bar{1}3\}$).

TBs on $(1\bar{2}10)$	E_{surf} (J/m^2)	E_{surf}/ρ (eV/atom)	Φ (eV)
TB1: $\{10\bar{1}1\}$	0.791	0.109	3.484
TB2: $\{10\bar{1}2\}$	0.807	0.110	3.477
TB3: $\{10\bar{1}3\}$	0.896	0.127	3.441
TB-free surface	0.742	0.102	3.467

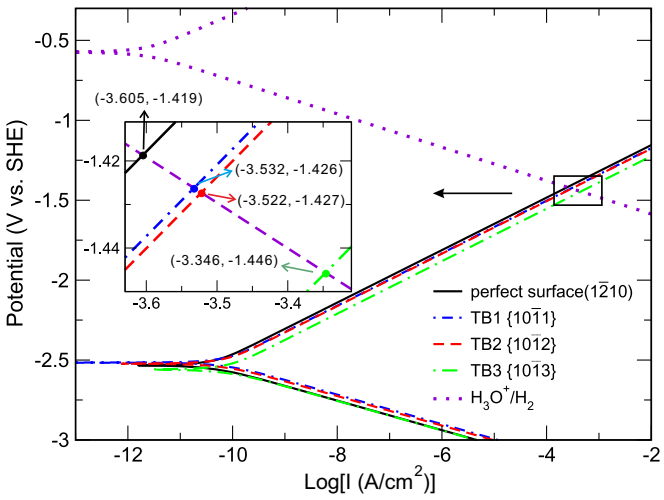

FIG. 3. Simulated anodic dissolution curves of the TB-containing (TB1 $\{10\bar{1}1\}$, TB2 $\{10\bar{1}2\}$, and TB3 $\{10\bar{1}3\}$) $(1\bar{2}10)$ surfaces in comparison with the TB-free $(1\bar{2}10)$ surface. For the depolarization reaction, we consider it as a hydrogen evolution reaction which was fitted from the known experimental results [19]. In particular, it needs to be mentioned that this hydrogen evolution reaction is here assumed to be independent of surface defects. All the polarizations of anodic dissolution were further referenced to the standard hydrogen electrode according to our proposed modeling [40].

TABLE III. The TB interface length per area (L_s^0) for the TB-containing surface supercell used here, the corresponding variations ($d^0_{\log I_{\rm corr}({\rm A/cm^2})}$) of corrosion current densities ($\log I_{\rm corr}({\rm A/cm^2})$), the changes ($d^0_{V_{\rm corr}}$) of corrosion potentials, and the increased multiples $T^0_{I_{\rm corr}} = 10^{d_{\log I_{\rm corr}}}$ of corrosion current densities ($I_{\rm corr}$) for the TB-containing surface supercell compared with the TB-free surface.

TBs on $(1\bar{2}10)$	L_s^0 (nm/nm^2)	$d^0_{\log I_{\rm corr}({\rm A/cm^2})}$	$T^0_{I_{\rm corr}}$	$d^0_{V_{\rm corr}}$ (mV)
$\{10\bar{1}1\}$	0.8147	0.073	$\times 1.18$	-7
$\{10\bar{1}2\}$	0.5310	0.083	$\times 1.21$	-8
$\{10\bar{1}3\}$	1.1282	0.259	$\times 1.82$	-27

TABLE IV. The variations ($d_{\log I_{\rm corr}({\rm A/cm^2})}$) of corrosion current densities ($\log I_{\rm corr}({\rm A/cm^2})$), the changes ($d_{V_{\rm corr}}$) of corrosion potentials ($V_{\rm corr}$), and the increased multiples $T_{I_{\rm corr}} = 10^{d_{\log I_{\rm corr}}}$ of corrosion current densities ($I_{\rm corr}$) for the TB-containing surface supercells compared with the TB-free surface, when the TB interface length per area for the three TB-containing surfaces are normalized to a given density of L_s.

TBs on $(1\bar{2}10)$	$d_{\log I_{\rm corr}({\rm A/cm^2})}$	$T_{I_{\rm corr}}$	$d_{V_{\rm corr}}$ (mV)
$\{10\bar{1}1\}$	$0.086L_s$	$\times 1.22^{L_s}$	$-8.3L_s$
$\{10\bar{1}2\}$	$0.156L_s$	$\times 1.43^{L_s}$	$-15.1L_s$
$\{10\bar{1}3\}$	$0.230L_s$	$\times 1.70^{L_s}$	$-23.9L_s$

were reported as a function of strains [19]. In terms of these experimental data, here we selected the observed hydrogen evolution reactions of the AM50 alloys in a pH = 9.7 solution as the cathodic depolarization reactions (Fig. 3) in our modeling. First, in the pH = 9.7 corrosive solution the equilibrium electrode potential of the hydrogen evolution reaction is -0.573 V_{SHE} according to the well-known Nernst equation. Second, a straight-line fitting on the Tafel line of the cathodic region from the measured polarization curve gives the Tafel slope to be 104 mV (namely, $\alpha \approx 0.43$ for the cathodic region). Adopting the equilibrium electrode potential of -0.573 V_{SHE}, we can derive the exchange current density of about $10^{-11.7}$ A/cm^2 for the hydrogen evolution reaction. With these treatments including a hydrogen evolution reaction as the depolarization reaction in Fig. 3, the corrosion current densities (in the unit of $\log[I_{\rm corr}/({\rm A/cm^2})]$) can be calculated to be -3.532, -3.522, and -3.346 for those TB-containing surfaces with TB1 $\{10\bar{1}1\}$, TB2 $\{10\bar{1}2\}$, and TB3 $\{10\bar{1}3\}$, respectively. These values are all larger than the value (-3.605) for the TB-free surface. Furthermore, in Table III we have compiled the corresponding variations ($d^0_{\log[I_{\rm corr}({\rm A/cm^2})]}$) of corrosion current densities ($\log[I_{\rm corr}({\rm A/cm^2})]$) and the changes ($d^0_{V_{\rm corr}}$) of corrosion potentials for the TB-containing surfaces with the TB interface length per area, L_s^0, compared with those of the ideal TB-free surface. It reveals that in the same corrosive solution the corrosion current densities ($I_{\rm corr}$) of the TB-containing surfaces are larger than that of the TB-free surface by $T^0_{I_{\rm corr}} = 10^{d^0_{\log I_{\rm corr}}}$, namely, about 1.18 to 1.82 times. Their corresponding corrosion potentials can be further determined to be -1.426 V_{SHE}, -1.427 V_{SHE}, and -1.446 V_{SHE}, which are all lower by about 7–27 mV than -1.419 V_{SHE} of the TB-free $(1\bar{2}10)$ surface. Importantly, the theoretically derived acceleration effects of TBs on the corrosion are consistent with experimental observations [18,19,24,26]. For instance [18], the transmission electron microscopy micrograph of the Mg-2.65wt.%Zn samples after compressive strains indicates the TB existence of the twinning system of $\{10\bar{1}1\}\langle 10\bar{1}2\rangle$. Furthermore, the corrosion tests in Hank's solution at 37 °C show that the corrosion current densities of Mg-2.65wt.%Zn samples with different compressive strains are larger by ∼2.86–13.81 times that of the sample without the deformation. Although the experimentally derived acceleration effect of TBs is higher than the theoretical results from the supercells used here, both experiments and theoretical calculations verify the fact that the existence of TBs increases the corrosion rate. Moreover, in the above experimental works the density of the deformed TB was unknown. As a result, one would be cautioned when directly comparing the different effects of TBs on the corrosion behaviors between experimental and calculated results.

It should be noted that the calculated effects of TBs on the corrosion behavior are indeed related to the sizes of supercells being used to simulate the TB-containing surfaces. It is thus reasonable to compare the effects of the three TBs when the densities of different TBs on the surface are renormalized to any given density. Within this context, for a TB-containing surface with a TB interface length per area in a given density of L_s, we have supposed that the variations ($d_{\log I_{\rm corr}}$) of corrosion current density caused by L_s can be derived through this relationship, $d_{\log I_{\rm corr}} = d^0_{\log I_{\rm corr}} \frac{L_s}{L_s^0}$, and the corresponding changes ($d_{V_{\rm corr}}$) of the corrosion potential can be further obtained by $d_{V_{\rm corr}} = d^0_{V_{\rm corr}} \frac{L_s}{L_s^0}$. Physically, this assumption is based on the fact that we believed that both corrosion current density and corrosion potential can be greatly affected by the same proportional rate of $\frac{d^0_{\log I_{\rm corr}}}{L_s^0}$ and $\frac{d^0_{V_{\rm corr}}}{L_s^0}$, respectively. According to the above assumptions we have further derived the increased multiple $T_{I_{\rm corr}} = 10^{d_{\log I_{\rm corr}}}$ of the corrosion current densities for the three TB-containing surfaces compared with the ideal TB-free surface, respectively, as shown in Table IV. In comparison with the ideal TB-free surface, the TB-containing surfaces have resulted in the higher corrosion current densities by 1.22^{L_s}, 1.43^{L_s}, and 1.70^{L_s} times for TB1, TB2, and TB3, respectively, and the corresponding changes of the corrosion potentials are $-8.3L_s$, $-15.1L_s$, and $-23.9L_s$ mV, respectively. In addition, from our current results the acceleration effect increases as in the sequence TB1 < TB2 < TB3.

Furthermore, we have calculated the charge density maps of the topmost atomic layer for the TB-free and the three TB-containing $(1\bar{2}10)$ surfaces. As shown in Fig. 4, the charge densities follow the regular pattern on the TB-free surface, whereas the charge densities are varied, sensitively, upon the distortions caused by the existence of TBs on the TB-containing surfaces. The existence of TBs on the surface obviously changes the bond lengths of the nearest-neighboring Mg atoms surrounding the TB, leading to the heterogeneous distribution of the charge densities. For the TB1- and TB3-containing surfaces, the bond lengths of the nearest-neighboring Mg atoms surrounding both TB1 and TB3 decrease, while for the TB2-containing surface these

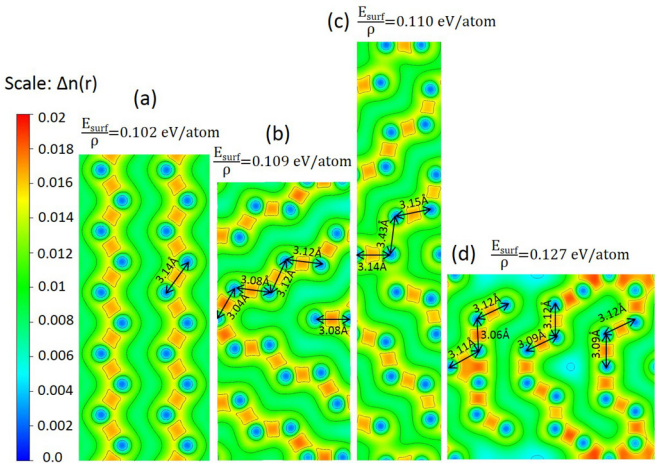

FIG. 4. The charge density maps of the (a) TB-free, (b) TB1-containing, (c) TB2-containing, and (d) TB3-containing $(1\bar{2}10)$ surfaces.

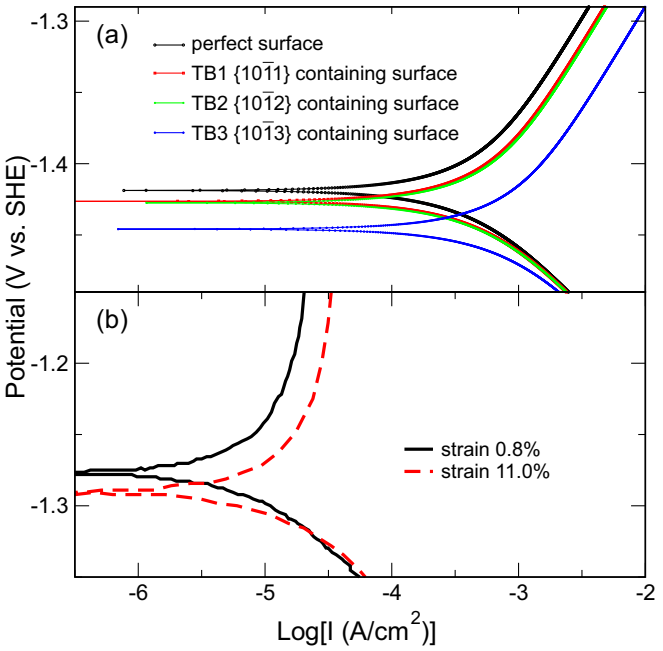

FIG. 5. Comparison between experimental and simulated apparent polarization curves. (a) Theoretically simulated apparent polarization curves for the $(1\bar{2}10)$ surfaces with the TBs $\{10\bar{1}1\}$, $\{10\bar{1}2\}$, and $\{10\bar{1}3\}$, in comparison with TB-free surface $(1\bar{2}10)$. (b) Experimentally measured polarization curves as a function of strain for AM50 alloy [19] in sodium tetraborate solution (pH = 9.7).

bond lengths increase to some degree. As discussed above, the surface energy densities for all three TB-containing surfaces are higher than the TB-free surface. This fact demonstrates that the TB existence on the surface makes the Mg atom less stable in energy. It is in agreement with the increase of the corrosion rate. The heterogeneous charge distribution induced by the disordered atoms surrounding the TBs is the substantial reason as to why the Mg atom on the TB-containing surfaces becomes less stable in energy and the corrosion rate increases.

Certainly, in our modeling we only focus on the anodic dissolution, assuming that the rate of hydrogen evolution reaction is the same for all TB-containing surfaces and independent of various surface defects. According to our modeling [40], the equilibrium electrode potential can be directly determined by the work function. The differences among the equilibrium electrode potentials of the anodic reaction for the TB-containing surfaces and the TB-free surface are very small (Fig. 3). This fact can be reflected well by the derived work functions in Table II. From Fig. 3, because the crossover between the polarization curve of the hydrogen evolution reaction and the anodic dissolution reaction curve occurs in the Tafel part, the surface energy density plays a leading role in determining the rate of anodic dissolution. This behavior has been theoretically analyzed in Eqs. (5) and (6).

By combining the anodic dissolution reaction and the depolarization reaction of the hydrogen evolution reaction in Fig. 3, the theoretical apparent polarization curves of three different TB-containing surfaces can be derived in Fig. 5(a). It can be seen that, with respect to the TB-free surface, the apparent polarization curves of the TB-containing surfaces obviously shift right and down, indicating a faster rate of the anodic dissolution behavior. In particular, for the TB3-containing surface this rate is even faster due to its higher surface energy. Importantly, we found that the currently derived apparent polarization curves for these TB-containing surfaces can be comparable with experimental observations. In the experimental case of AM50 alloy [19] in Fig. 5(b), the apparent polarization curves obviously have a right and down shifting with increasing the deformation from 0.8% to 11.0%. These consistent results reveal that the occurrence of different deformed twin boundaries takes an important role in the deteriorated corrosion behavior under different strains. Note that the relative positions between the theoretical curves and the experimental curves exhibit some differences, which can be attributed to three facts. The first factor is the alloying effect. Our current calculations have referred to a pure Mg metal and have not considered the existence of an oxidation film. However, in the AM50 alloys, Al and Mn are alloyed elements which both influence the corrosion behaviors [19]. The second factor is that only one type of TB is considered in each case of our calculations, but various dislocations and deformation twins often exist in real AM50 alloy samples under strains. The third factor is the position of the TBs. In our modeling we have only considered that the TB planes are perpendicular to the surface, which is, of course, a simplified situation in practice.

Experiments usually observed that microscopic galvanic corrosion occurs in the region between the grain boundaries and the grains. This kind of behavior can be theoretically inferred to occur in the region between the twin boundaries and the grains, according to our current calculations. For a TB-free $(1\bar{2}10)$ crystal surface of Mg, both the anodic dissolution reaction and the cathodic hydrogen evolution reaction determine its corrosion rate. The corrosion potential and current density are marked by point A in Fig. 6. However, when a twin boundary (i.e., TB1 $\{10\bar{1}1\}$) is included in this surface, both the corrosion potential and current density are transferred to a faster point of B in Fig. 6. This transformation was mainly because the existence of the twin boundary increases the

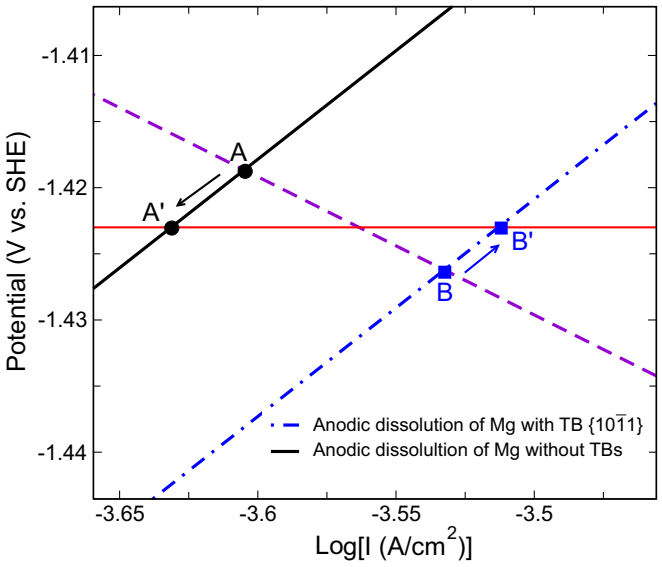

FIG. 6. Changes of the corrosion potential and corrosion current density of the twin boundary region and perfect grain surface due to microscopic galvanic interactions between surface twin boundaries and grains. The red line between points A and B indicates the overall corrosion potential of a sample due to coupling of the twin boundary and untwin grains.

surface energy density. Once the surface has twin boundaries, due to the coupling between the twin boundaries and the grains its overall corrosion potential will be in between the potentials of point A and point B, as shown by an arbitrary red line in Fig. 6. This fact means that, at this overall potential marked by the red line, the anodic dissolution rate at the twin boundary region speeds up from point B to point B′, whereas the anodic dissolution rate of the grain will slow down from point A to point A′. As a result, the so-called microscopic galvanic corrosion occurs between the twin boundaries and grains on the surface of the sample. It will thereby accelerate the corrosion rate of the grain boundary region and slow down the corrosion rate of the grains.

In order to analyze the influences of alloying elements on the corrosion behaviors of TB-containing surfaces of magnesium alloys, we have further considered some common alloying elements (i.e., Al, As, Cd, Cr, Ga, Hg, Mn, Zn, Zr, Sn, and Y) in our modeling. It needs to be emphasized that we have only considered the case in which the alloying elements locate at the topmost layer [71–73]. It is mainly because, if the alloying elements are in the inner layers of these slab modelings, their influences are indeed very close to those in bulk systems. To study the effect of alloying addition on corrosion behaviors, it is certainly important to see the alloying effect with the elemental addition at the topmost layer. Here, we only selected the TB1-containing surface slab modeling as the platform to study the effects of these alloying additions, because the TB1 twin boundary on the $(1\bar{2}10)$ surface is not only the most stable one in energy but also is the often experimentally observed one in magnesium alloys. We have first calculated the segregation energies of these selected alloying elements (X) by varying three different substitution sites, sites 1 and 2 at the TB on the surface as

TABLE V. DFT-derived segregation energies $[E_{\rm seg}^{\rm TB}(X)]$ for alloying elements (X) replacing site 1 or 2 on the TB1-containing $(1\bar{2}10)$ surface, and the segregation energies $[E_{\rm seg}^{\rm surf}(X)]$ on the TB-free $(1\bar{2}10)$ surface. The calculated work functions (Φ) of these three cases are also included.

	Site 1 (eV)		Site 2 (eV)		TB-free (eV)	
X	$E_{\rm seg}^{\rm TB}(X)$	Φ	$E_{\rm seg}^{\rm TB}(X)$	Φ	$E_{\rm seg}^{\rm surf}(X)$	Φ
Al	−0.072	3.499	+0.054	3.515	+0.035	3.486
As	−0.859	3.478	−0.737	3.511	−0.747	3.470
Cd	−0.177	3.492	−0.087	3.500	−0.103	3.475
Cr	+0.869	3.502	+1.099	3.504	+1.037	3.493
Ga	−0.241	3.495	−0.130	3.513	−0.138	3.483
Hg	−0.294	3.488	−0.180	3.502	−0.192	3.478
Mn	+0.532	3.484	+0.868	3.508	+0.812	3.473
Zn	−0.209	3.477	−0.097	3.495	−0.113	3.470
Zr	+1.458	3.464	+1.343	3.451	+1.325	3.450
Sn	−0.436	3.503	−2.477	3.518	−2.514	3.486
Y	+0.685	3.415	+0.356	3.402	−4.105	3.398

marked in Fig. 2(a) and any substitution site on the surface without any TB. Sites 1 and 2 mean that X locates at the twin boundary of TB1 $\{10\bar{1}1\}$ on the $(1\bar{2}10)$ surface, whereas the third substitution site corresponds to the position within the grains of a specified $(1\bar{2}10)$ surface. According to the definitions in Eqs. (6) and (7), we have derived the segregation energies of these alloying elements upon these three different sites considered here in Table V.

In order to visualize the changes of different alloying elements upon different sites, we have plotted the calculated segregation energies $[E_{\rm seg}^{\rm TB}(X)]$ of sites 1 and 2 of the TB1-containing surface and the segregation energies $[E_{\rm seg}^{\rm surf}(X)]$ on the TB1-free $(1\bar{2}10)$ surface in Fig. 7. The segregation energies of alloyed Cr, Mn, and Zr on the TB1-containing or the TB-free surfaces are highly positive, indicating that these alloyed atoms tend to move away from the $(1\bar{2}10)$ surface regardless of whether or not the surface has TBs. Different from Cr, Mn, and Zr, the situation of Al is a bit complicated. When Al locates at the TB1-free $(1\bar{2}10)$ surface or site 2 on the TB1-containing surface, its segregation energy is slightly above zero, while at site 1 on the TB1-containing surface the segregation energy is slightly below zero (Fig. 7). In contrast, the segregation energies of some other alloying elements are all negative. For Al, As, Ga, Zn, and Hg alloying elements, they prefer to occupy site 1 at the twin boundary of the TB1-containing surface. In particular, for both Sn and Y, they prefer to locate within the grains because their segregation energies in the TB1-free surface are as negative as −2.514 and −4.105 eV, respectively.

With these alloying additions, we have further calculated their surface energy densities ($E_{\rm surf}/\rho$), which is one of the most important parameters of our corrosion modeling [40], for the TB1-containing or TB1-free $(1\bar{2}10)$ surfaces where alloying elements (X = Al, As, Cd, Ga, Hg, Zn, and Sn) locate at three selected sites in Fig. 8. For X = As, Cd, Hg, Zn, and Sn alloying atoms, the X-alloyed surface energy densities

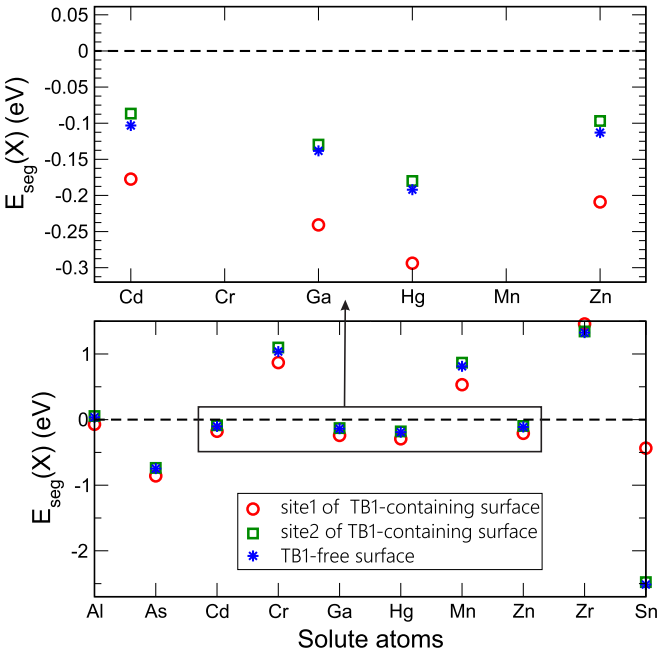

FIG. 7. DFT-derived segregation energies $[E_{seg}^{TB}(X)]$ for alloying elements (X) located at sites 1 and 2 on the TB1-containing $(1\bar{2}10)$ surface, and the segregation energies $[E_{seg}^{surf}(X)]$ on the TB1-free $(1\bar{2}10)$ surface.

are all lower than those of corresponding X-free surfaces. This fact demonstrates that their solutions will slow down the anodic dissolution rate, consequently enhancing the corrosion resistance of those X-alloyed magnesium alloys. This conclusion is basically in good agreement with some known experimental facts [9,74–78], although in those experiments the twins were not clearly discussed. When Al alloying is added at sites 1 or 2 of the TB1-containing surface, the surface energy density is lower than the Al-free TB1-containing surface. It means that the segregation of Al at sites 1 or 2 on the grain boundary potentially reduces the anodic dissolution rate of TB-containing surface. However, the surface energy density of the Al-alloyed but TB1-free surface is a bit higher than the Al-free and TB1-free surface, indicating that Al segregation on the TB-free surface, rather than on the TBs, will possibly accelerate the anodic dissolution rate. From our current calculations, Al energetically prefers to locate at site 1 of the twin boundary of the TB-containing surface. This fact suggests that Al has the functionality to potentially enhance the corrosion-resistant behavior. In practice, it is possible for Al to simultaneously exist both at the twin boundaries and in the grain bulk. With this situation, the difference in the corrosion rate between the twin boundary region and the grain bulk will be decreased, which reduces the tendency of the microscopic galvanic corrosion between the grain boundary and the grain bulk. A similar situation has been observed in the case of the Ga alloyed surface. The only difference between Ga and Al is that its energy is slightly higher than that of the X-free but TB1-containing surface when Ga locates at site 2 of the twin boundary.

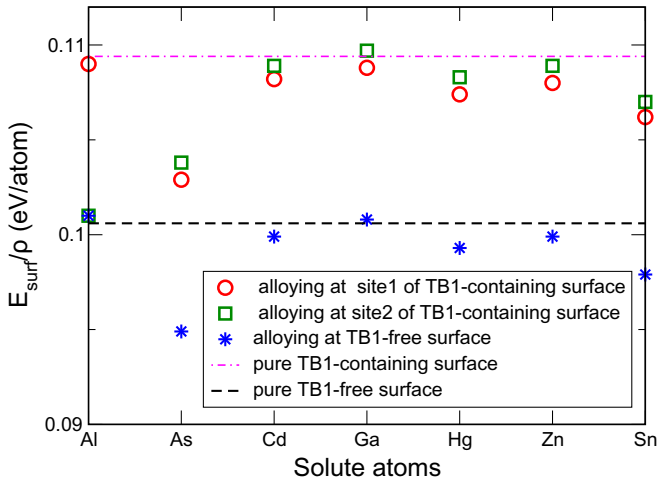

FIG. 8. DFT-derived surface energy densities (E_{surf}/ρ) for the alloyed TB1-containing $(1\bar{2}10)$ surface, where alloying elements (X) are located at sites 1 or 2 at the TB1 twin boundary, and at the TB1-free $(1\bar{2}10)$ surface, as compared with the X-free, and TB1-free or TB1-containing $(1\bar{2}10)$ surface.

Finally, we would like to emphasize that the current work aims to interpret the intrinsic mechanism of the accelerating effect of the TB itself on corrosion in magnesium alloys, and further to analyze the effects of alloying elements on the corrosion resistance. This theoretical work is not a simulation in a real corrosive environment. One should be always cautioned when directly comparing our current calculations with various available experiment results: (i) in our modeling, alloying elements were considered to be a solid solution in the Mg matrix rather than the formation of intermetallic particles; (ii) the current work has not taken into account the effects of various oxides or atomic arrangements, such as steps, kinks, and reconstructions, on surfaces; and (iii) the current modeling has only considered the basic process of the anodic dissolution and the hydrogen evolution reaction has been assumed as the only kind of cathodic reaction.

III. CONCLUSIONS AND REMARKS

Through first-principles calculations we have theoretically investigated the effects of twin boundaries on the anodic dissolution of Mg metal in a pH = 9.7 solution. The main conclusions are summarized:

(i) For pure Mg, the calculated energies of the three twin boundaries TB1 $\{10\bar{1}1\}$, TB2 $\{10\bar{1}2\}$, and TB3 $\{10\bar{1}3\}$ are 85.56, 111.94, and 209.92 mJ/m^2, respectively.

(ii) The three twin boundaries (TB1 $\{10\bar{1}1\}$, TB2 $\{10\bar{1}2\}$, and TB3 $\{10\bar{1}3\}$) calculated here speed up the corrosion rate of Mg by about 1.18–1.82 times. The corresponding corrosion potentials are lower by about 7–27 mV than that of the TB-free $(1\bar{2}10)$ surface. The accelerating multiples of the corrosion current density are related to the TB interface length per area.

(iii) The alloying additions (As, Cd, Hg, Zn, and Sn) will slow down the anodic dissolution rate of Mg, thereby enhancing the corrosion resistance of magnesium alloys.

In addition, we still need to remark on two aspects. First, although the TB is very common in the deformation samples,

inevitably there are also other defects, such as dislocations. From the viewpoint of the experiments, it is nearly impossible to identify the exact impact of a single TB on the corrosion of Mg and Mg-based alloys. Fortunately, we can evaluate the accelerating effect of a kind of deformation-induced TB on the corrosion from the DFT calculation through our currently proposed corrosion modeling. This work not only illustrates the specific effect of the three TBs on the corrosion behaviors of Mg, but also unfolds the coupling effect of the alloying element and the TB on the corrosion of Mg. Second, this method provides an accessible tool to investigate the influences of various defects (including but not limited to TBs) on anodic dissolution behaviors, only with necessary first-principles inputs including defects considered in modeling. The modeling calculations can interpret the experimentally observed results and help to investigate the potential corrosion-resistant properties of materials. Furthermore, this method still provides an accessible way to investigate the impact factors on the corrosion for a given alloy.

ACKNOWLEDGMENTS

This work was supported by the National Science Fund for Distinguished Young Scholars (Grant No. 51725103), by the Science Challenging Project No. TZ2016004 and by the National Key Research and Development Program of China (Grant No. 2017YFB0702302). All calculations have been performed on the high-performance computational cluster in the Shenyang National University Science and Technology Park.

[1] W. Xu, N. Birbilis, G. Sha, Y. Wang, J. E. Daniels1, Y. Xiao, and M. Ferry, Nat. Mater. **14**, 1229 (2015).
[2] A. Luo and M. O. Pekguleryuz, J. Mater. Sci. **29**, 5259 (1994).
[3] F. H. Froes, D. Eliezer, and E. L. Aghion, JOM **50**, 30 (1998).
[4] A. E. Coy, F. Viejo, P. Skeldon, and G. E. Thompson, Corros. Sci. **52**, 3896 (2010).
[5] S. D. Wang, D. K. Xu, X. B. Chen, E. H. Han, and C. Dong, Corros. Sci. **92**, 228 (2015).
[6] M. Mondeta, E. Barraud, S. Lemonnier, J. Guyon, N. Allain, and T. Grosdidierb, Acta Mater. **119**, 55 (2016).
[7] M. Habibnejad-korayem, M. K. Jain, H. S. Zuro, and R. K. Mishra, Acta Mater. **113**, 155 (2016).
[8] W. F. Xu, Y. Zhang, L. M. Peng, W. J. Ding, and J. F. Nie, Acta Mater. **84**, 317 (2015).
[9] G. L. Song and A. Atrens, Adv. Eng. Mater. **1**, 11 (1999).
[10] G. L. Makar and J. Kruger, Int. Mater. Rev. **38**, 138 (1993).
[11] S. Virtanen, Mater. Sci. Eng. B **176**, 1600 (2011).
[12] A. Pardo, M. C. Merino, A. E. Coy, R. Arrable, F. Viejo, and E. Matykina, Corros. Sci. **50**, 823 (2008).
[13] N. T. Kirkland, N. Birbilis, and M. P. Staiger, Acta Biomater. **8**, 925 (2012).
[14] R. L. Xin, Y. M. Luo, A. L. Zuo, J. C. Gao, and Q. Liu, Mater. Lett. **72**, 1 (2012).
[15] B. Wang, X. H. Chen, F. S. Pan, and J. J. Mao, Prog. Nat. Sci.: Mater. Int. **27**, 695 (2017).
[16] H. C. Pan, F. S. Pan, X. Wang, J. Peng, J. Gou, J. She, and A. T. Tang, Int. J. Thermophys. **34**, 1336 (2013).
[17] S. Q. Luo, A. T. Tang, F. S. Pan, K. Song, and W. Q. Wang, Trans. Nonferrous Met. Soc. China **21**, 795 (2011).
[18] Y. Zheng, Y. Li, J. H. Chen, and Z. Y. Zou, Corros. Sci. **90**, 445 (2015).
[19] M. Andrei, A. Eliezer, P. L. Bonora, and E. M. Gutman, Mater. Corros. **53**, 455 (2002).
[20] D. Song, A. B. Ma, J. H. Jiang, P. H. Lin, D. H. Yang, and J. F. Fan, Corros. Sci. **53**, 362 (2011).
[21] P. L. Bonora, M. Andrei, A. Eliezer, and E. M. Gutman, Corros. Sci. **44**, 729 (2002).
[22] B. J. Wang, D. K. Xu, J. H. Dong, and W. Ke, Scr. Mater. **88**, 5 (2014).
[23] G. L. Song and Z. Q. Xu, Electrochim. Acta **55**, 4148 (2010).
[24] N. N. Aung and W. Zhou, Corros. Sci. **52**, 589 (2010).
[25] W. C. Neil, M. Forsyth, P. C. Howlett, C. R. Hutchinson, and B. R. W. Hinton, Corros. Sci. **51**, 387 (2009).
[26] D. Song, A. B. Ma, J. Jiang, P. H. Lin, D. H. Yang, and J. F. Fan, Corros. Sci. **52**, 481 (2010).
[27] J. F. Nie, Y. M. Zhu, J. Z. Liu, and X. Y. Fang, Science **340**, 957 (2013).
[28] G. L. Song and Z. Q. Xu, Corros. Sci. **54**, 97 (2012).
[29] J. Chen, J. H. Dong, J. Q. Wang, E. H. Han, and W. Ke, Corros. Sci. **50**, 3610 (2008).
[30] R. L. Liu, M. F. Hurley, A. Kvryan, G. Williams, J. R. Scully, and N. Birbilis, Sci. Rep. **16**, 28747 (2016).
[31] R. L. Liu, J. R. Scully, G. Williams, and N. Birbilis, Electrochim. Acta **260**, 184 (2018).
[32] M. Nezafati, K. Cho, A. Giri, and C.-S. Kim, Mater. Chem. Phys. **182**, 347 (2016).
[33] K. S. Williams, V. Rodriguez-Santiago, and J. W. Andzelm, Electrochim. Acta **210**, 261 (2016).
[34] D. Kecik and M. K. Aydinol, Surf. Sci. **603**, 304 (2009).
[35] H. Lei, C. Wang, Y. Yao, Y. Wang, M. Hupalo, D. McDougall, M. Tringides, and K. Ho, J. Chem. Phys. **139**, 224702 (2013).
[36] M. Nezafati, I. Sohn, J. B. Ferguson, J.-S. Park, K. Cho, and C.-S. Kim, Comp. Mater. Sci. **105**, 18 (2015).
[37] Y. H. Duan, S. G. Zhou, Y. Sun, and M. J. Peng, Comput. Mater. Sci. **84**, 108 (2014).
[38] K. Hagihara, M. Okubo, M. Yamasaki, and T. Nakano, Corros. Sci. **109**, 68 (2016).
[39] G. L. Song, R. Mishra, and Z. Q. Xu, Electrochem. Commun. **12**, 1009 (2010).
[40] H. Ma, X.-Q. Chen, R. H. Li, S. L. Wang, J. H. Dong, and W. Ke, Acta Mater. **130**, 137 (2017).
[41] T. Hammerschmidt, P. Vogl, and A. Kersch, Phys. Rev. B **71**, 205409 (2005).
[42] J. P. Simon, J. Phys. F: Metal Phys. **10**, 337 (1980).
[43] Y. Wang, L. Q. Chen, Z. K. Liu, and S. N. Mathaudhu, Scr. Mater. **62**, 646 (2010).
[44] J. Zhang, Y. C. Dou, and Y. Zheng, Scr. Mater. **80**, 17 (2014).
[45] L. Huber, J. Rottler, and M. Militzer, Acta Mater. **80**, 194 (2014).
[46] P. Hohenberg, Phys. Rev. **136**, B864 (1964).
[47] W. Kohn and L. J. Sham, Phys. Rev. **140**, A1133 (1965).
[48] G. Kresse and J. Hafner, Phys. Rev. B **47**, 558 (1993).

[49] G. Kresse and J. Furthmüller, Phys. Rev. B **54**, 11169 (1996).
[50] P. E. Blöchl, Phys. Rev. B **50**, 17953 (1994).
[51] J. P. Perdew, K. Burke, and M. Ernzerhof, Phys. Rev. Lett. **77**, 3865 (1996).
[52] J. R. Morris, Y. Ye, and M. H. Yoo, Philos. Mag. **85**, 233 (2005).
[53] H. J. Monkhorst and J. D. Pack, Phys. Rev. B **13**, 5188 (1976).
[54] H. L. Skriver and N. M. Rosengaard, Phys. Rev. B **46**, 7157 (1992).
[55] H. Song, M. Zhao, and J. Li, Mod. Phys. Lett. B **30**, 1650152 (2016).
[56] G. Laplanche, A. Kostka, O. M. Horst, G. Eggeler, and E. P. George, Acta Mater. **118**, 152 (2016).
[57] L. Remy, Acta Metall. **26**, 443 (1978).
[58] R. L. Fullman, Trans. AIME **197**, 447 (1953).
[59] G. L. Song, JOM **64**, 671 (2012).
[60] S. Trasatti, Electrochim. Acta **35**, 269 (1990).
[61] G. L. Makar and J. Kruger, J. Electrochem. Soc. **137**, 414 (1990).
[62] G. R. Hoey and M. Cohen, J. Electrochem. Soc. **105**, 245 (1958).
[63] R. L. Petty, A. W. Davidson, and J. Kleinberg, J. Am. Chem. Soc. **76**, 363 (1954).
[64] M. D. Rausch, W. E. McEwen, and J. Kleinberg, J. Am. Chem. Soc. **76**, 3622 (1954).
[65] G. Galicia, N. Pébère, B. Tribollet, and V. Vivier, Corros. Sci. **51**, 1789 (2009).
[66] G. Baril, G. Galicia, C. Deslouis, N. Pébère, B. Tribollet, and V. Vivier, J. Electrochem. Soc. **154**, C108 (2007).
[67] S. Thomas, N. V. Medhekar, G. S. Frankel, and N. Birbilis, Curr. Opin. Solid State Mater. Sci. **19**, 85 (2015).
[68] N. T. Kirkland, G. Williams, and N. Birbilis, Corros. Sci. **65**, 5 (2012).
[69] W. Bollmann, *Crystal Defects and Crystalline Interfaces* (Springer-Verlag, New York, 1970).
[70] G. Gottstein, *Physical Foundations of Materials Science* (Springer-Verlag, New York, 2004).
[71] Z. Fang, J. Wang, X. Yang, Q. Sun, Y. Jia, H. Liu, T. Xi, and S. Guan, Appl. Surf. Sci. **409**, 149 (2017).
[72] P. Banerjee and G. P. Das, AIP Conf. Proc. **1731**, 080028 (2016).
[73] J. A. Yuwono, N. Birbilis, K. S. Williams, and N. V. Medhekar, J. Phys. Chem. C **120**, 26922 (2016).
[74] Z. Shi, G. Song, and A. Atrens, Surf. Technol. **201**, 492 (2006).
[75] S. N. Xu, M. E. Ikpi, J. H. Dong, J. Wei, W. Ke, and N. Chen, Int. J. Electrochem. Sc. **7**, 4735 (2012).
[76] R. Shabadi, R. Ambat, and E. S. Dwarakadasa, Mater. Des. **53**, 445 (2014).
[77] Y. Feng, R. Wang, K. Yu, C. Q. Peng, and W. Li, Trans. Nonferrous Met. Soc. China **17**, 1363 (2007).
[78] N. Birbilis, G. Williams, K. Gusieva, A. Samaniego, M. A. Gibson, and H. N. McMurray, Electrochem. Commun. **34**, 295 (2013).